

Stellar Characterization and a Chromospheric Activity Analysis of a K2 Sample of Planet-Hosting Stars

V. LOAIZA-TACURI ¹, KATIA CUNHA ^{1,2}, VERNE V. SMITH ³, F. QUISPE-HUAYNASI ¹, ELLEN COSTA-ALMEIDA,¹
LUAN GHEZZI,⁴ AND JORGE MELENDEZ⁵

¹*Observatório Nacional, Rua General José Cristino, 77, 20921-400 São Cristóvão, Rio de Janeiro, RJ, Brazil*

²*Steward Observatory, University of Arizona, 933 North Cherry Avenue, Tucson, AZ 85721, USA*

³*NSF's NOIRLab, 950 North Cherry Avenue, Tucson, AZ 85719, USA*

⁴*Universidade Federal do Rio de Janeiro, Observatório do Valongo, Ladeira do Pedro Antônio, 43, Rio de Janeiro, RJ 20080-090, Brazil*

⁵*Instituto de Astronomia, Geofísica e Ciências Atmosféricas, Universidade de São Paulo, Rua do Matão 1226, São Paulo 05508-090, Brazil*

(Received 17-Jan, 2024; Revised 01-May, 2024; Accepted 09-May, 2024)

Submitted to ApJ

ABSTRACT

Effective temperatures, surface gravities, and iron abundances were derived for 109 stars observed by the K2 mission using equivalent width measurements of Fe I and Fe II lines. Calculations were carried out in LTE using Kurucz model atmospheres. Stellar masses and radii were derived by combining the stellar parameters with Gaia DR3 parallaxes, V-magnitudes, and isochrones. The derived stellar and planetary radii have median internal precision of 1.8%, and 2.3%, respectively. The radius gap near $R_{\text{planet}} \sim 1.9R_{\oplus}$ was detected in this K2 sample. Chromospheric activity was measured from the Ca II H and K lines using the Values of $\log R'_{\text{HK}}$ were investigated as a function of stellar rotational period (P_{rot}) and we found that chromospheric activity decreases with increasing P_{rot} , although there is a large scatter in $\log R'_{\text{HK}}$ (~ 0.5) for a given P_{rot} . Activity levels in this sample reveal a paucity of F & G dwarfs with intermediate activity levels (Vaughan-Preston gap). The effect that stellar activity might have on the derivation of stellar parameters was investigated by including magnetically-sensitive Fe I lines in the analysis and we find no significant differences between parameters with and without magnetically-sensitive lines, although the more active stars ($\log R'_{\text{HK}} > -5.0$) exhibit a larger scatter in the differences in T_{eff} and $[\text{Fe}/\text{H}]$.

Keywords: (stars:) planetary systems — stars: fundamental parameters — stars: stellar activity — techniques: spectroscopic, parallaxes

1. INTRODUCTION

Currently there are ~ 5500 confirmed exoplanets (NASA Exoplanet Archive) orbiting more than 4250 host stars, with the majority of detections resulting from planetary transits, the largest number of which were observed by the Kepler mission (Borucki et al. 2010; Koch et al. 2010; Borucki 2016) and the extended Kepler mission, known as K2 (Howell et al. 2014), as well as the CoRoT mission (Deleuil et al. 2000, 2018). The

growing number of exoplanets has led to numerous studies whose main goals have been the characterization of planet-hosting stars and the planets orbiting them. Results from these studies have revealed fascinating patterns, such as the correlation between stellar metallicity and the frequency of giant planets (Gonzalez 1997; Fischer & Valenti 2005; Ghezzi et al. 2018, and subsequent studies), the absence of planets having sizes between the super-Earth and sub-Neptune regimes (Fulton et al. 2017; Fulton & Petigura 2018), known as the radius valley, and a slope in the value of the radius valley as a function of planetary orbital period (Van Eylen et al. 2018; Martinez et al. 2019, among others); such conclusions

provide constraints on planetary formation theories (e.g. [Ida & Lin 2004a,b, 2005](#); [Nayakshin 2010](#); [Mordasini et al. 2012, 2015](#); [Owen & Murray-Clay 2018](#); [Venturini et al. 2020](#)). The discovery of a planet-radius valley and its change as a function of orbital period was made possible thanks to high-precision spectroscopic methods used to determine the parameters and physical properties (effective temperature, T_{eff} , surface gravity, $\log g$, and metallicity, $[\text{Fe}/\text{H}]$) of the planet-hosting stars. The derived planetary radii depend most strongly on the radii of their host-stars coupled with the transit depths, with the stellar radii derived from the stellar parameters, thus precise stellar characterization is critical to the derivation of precise planetary radii.

An additional stellar property that can impact derived stellar and planetary radii is magnetic activity on the host star ([Yana Galarza et al. 2019](#); [Spina et al. 2020](#)), as it can influence the characterization of the host star and, thus, the planets orbiting it. This influence arises from the connections between planetary properties, such as radius and mass, and those of their parent stars. The intensity of stellar magnetic activity can manifest itself in features such as spots and flares, or chromospheric UV, X-ray, and radio emission ([Han et al. 2023](#)). Emission lines such as the cores of Ca II H and K, Mg II, H- α , the IR triplet of Ca II, and others are commonly used as indicators of chromospheric activity (or chromospheric emission). Among these indicators, the Ca II H ($\lambda 3968\text{\AA}$) and K ($\lambda 3934\text{\AA}$) lines, which originate in the photosphere, are commonly used as they are sensitive to chromospheric activity, which itself is associated with magnetic fields ([Leighton 1959](#); [Skumanich et al. 1975](#)). When a star has an active chromosphere, the cores of these very strong Ca II absorption lines undergo reversals, due to the chromospheric temperature increase, and become core emission features which appear in sharp contrast to the deep photospheric absorption, making them excellent diagnostic tools for assessing chromospheric activity.

In this study we derive stellar parameters for a sample of planet-hosting stars discovered by the K2 mission via a quantitative high-resolution spectroscopic analysis based on a set of carefully vetted Fe I and Fe II lines.

As part of the analysis, we also derive chromospheric activity levels by using the Ca II H and K lines and investigate the impact that stellar activity might have on spectroscopically-derived stellar parameters.

This paper is organized as follows: Section 2 provides details on the observations and data reduction. Section 3 discusses the methodology used to derive key stellar parameters and uncertainties, including effective temperatures, surface gravities, iron abundances (which can be taken as proxies for metallicities), stellar masses, radii, and planetary radii. In Section 4 we explain the approach used to assess stellar activity using the calcium H and K lines and in Sections 5 and 6 present discussions and conclusions, respectively.

2. DATA

The sample consists of host-stars observed by the Kepler extended mission (K2) during the C0 – C8 campaigns. The optical spectra of these stars were obtained from the California Planet Search (CPS) program, which used the HIGH Resolution Echelle Spectrometer (HIRES; [Vogt et al. 1994](#)) on the Keck I 10m telescope. These spectra were observed during observational campaigns carried out after August 2004, with the updated HIRES CCDs, and cover the wavelength range from $\lambda 3640\text{\AA}$ - 7990\AA , which includes the Ca II H and K lines.

Reduced HIRES spectra for a sample of 145 stars (one spectrum per star) were obtained from ExoFop¹ ([ExoFOP 2019](#)). These spectra were carefully inspected and 109 of them had signal-to-noise high enough in order to be analyzed for the derivation of stellar parameters and metallicities (Section 3). As it was of interest to have as many observations as possible per star to study stellar activity, 725 spectra were obtained from the Keck Observatory Archives² (KOA; [J. O’Meara 2020](#)), which were then used to measure the Ca II H and K lines located in the blue spectral region (Section 4). Observational data, such as identifiers, positions, B and V magnitudes (taken from the EPIC catalog and the NASA Exoplanet Archive), and K2 observational campaigns information of the sample stars are given in Table 1.

¹ <https://exofop.ipac.caltech.edu/tess/>

² <https://nexsci.caltech.edu/archives/koa/>

Table 1. Sample K2 Stars

ID	Host Name	R.A.	Decl.	<i>B</i>	<i>V</i>	Camp
		(deg)	(deg)	(mag)	(mag)	
EPIC211319617	K2-180	126.463933	10.246968	13.334	12.601	C5
EPIC211331236	K2-117	133.855682	10.469131	16.137	14.655	C5
EPIC211342524	...	128.098694	10.677239	13.052	12.422	C5
EPIC211351816	K2-97	127.762836	10.847586	13.770	12.611	C5
EPIC211355342	K2-181	127.554034	10.910294	13.494	12.749	C5
...

NOTE—This table is published in its entirety in the machine readable format. A portion is shown here for guidance regarding its form and content.

3. STELLAR PARAMETERS

The spectroscopic stellar parameters of effective temperature (T_{eff}), surface gravity ($\log g$), iron abundance ($A(\text{Fe})^3$), and microturbulent velocity (ξ), were derived by enforcing the excitation/ionization balances of a selected set of Fe I and Fe II equivalent widths. The analysis assumes local thermodynamic equilibrium (LTE) and uses 1-D plane parallel model atmospheres from the Kurucz ATLAS9 ODFNEW grid (Castelli & Kurucz 2003).

The line list used in this study was adopted from Yana Galarza et al. (2019), which is based on the line list of Meléndez et al. (2014); it contains 61 Fe I and 13 Fe II lines. Yana Galarza et al. (2019) provide a critical discussion of which Fe I and Fe II lines are most sensitive, along with those that are not sensitive, to magnetic activity through the combination of magnetic susceptibility, as measured by the Landé g -factor (g_L), and the line strength, as measured by the equivalent width. Table 2 lists the wavelengths of the Fe I (species=26.0) and Fe II (species=26.1) lines along with their excitation potentials, $\log gf$ values (both solar and from laboratory), and whether the line is classified as magnetically sensitive (Y) or not (N) by Yana Galarza et al. (2019). In the last column of Table 2 we show the equivalent widths (EWs) measured for the Solar spectrum (see discussion about the solar abundance determination below). We used the ARES code v2 (Sousa et al. 2015) to set the continuum and measure the EWs of all Fe lines in this study. Three line-free spectral regions: λ 5764 – 5766 Å, λ 6047 – 6052 Å, and λ 6068 – 6076 Å were used to set the continuum level. In this section we only consider in the analysis Fe lines which are deemed as insensitive to stellar activity. (An analysis including sensitive lines will be discussed in Section 5.1.4).

The spectroscopic methodology adopted here is similar to that used in our previous study of K2 targets (Loaiza-Tacuri et al. 2023), which used an automated code for the determinations of stellar parameters and metallicities named *qoyllur-quipu*⁴ or q^2 (Ramírez et al. 2014). Briefly, q^2 uses an input iron line list and measured equivalent widths in combination with the 2019 version of the abundance analysis code MOOG (Snedden 1973) to compute iron abundances, effective temperatures, surface gravities and metallicities. The iterative process begins with an interpolated model atmosphere calculated for assumed values of T_{eff} , $\log g$, and metallicity. Values of T_{eff} / $\log g$ / $A(\text{Fe})$ are adjusted iteratively (increased or decreased) to minimize trends $A(\text{Fe I})$ and $A(\text{Fe II})$ as functions of T_{eff} , $\log g$, and ξ until a solution is found for a final adjusted set of spectroscopic parameters of each star.

As a test to our methodology we analyzed solar-proxy spectra obtained with the HIRES spectrograph, focusing on reflected solar light from the asteroid Iris. The parameters and metallicities obtained for the solar proxy Iris were: $T_{\text{eff}} = 5744 \pm 33$ K, $\log g = 4.52 \pm 0.05$, $A(\text{Fe}) = 7.39 \pm 0.02$, and $\xi = 1.12 \pm 0.13$ km.s⁻¹; these are in general agreement with the solar parameters, indicating that our methodology does not likely have strong biases for solar-type stars. We note, however, that the mean metallicity for the solar proxies of $A(\text{Fe}) = 7.39$ is slightly more metal-poor than the Asplund et al. (2021) ($A(\text{Fe})_{\odot} = 7.46$) scale, keeping in mind that they obtain $A(\text{Fe}) < 7.40$ when they analyze in 1D.

The derived effective temperatures, surface gravities, metallicities, and microturbulent velocities for all analyzed stars are presented in Table 3. We show the stellar parameters of T_{eff} and $\log g$ for the K2 stars in this study in the Kiel diagram presented in Figure 1. The target stars are shown as filled circles color-coded by

³ $A(\text{X}) = \log(N(\text{X})/N(\text{H})) + 12.0$

⁴ <https://github.com/astroChasqui/q2>

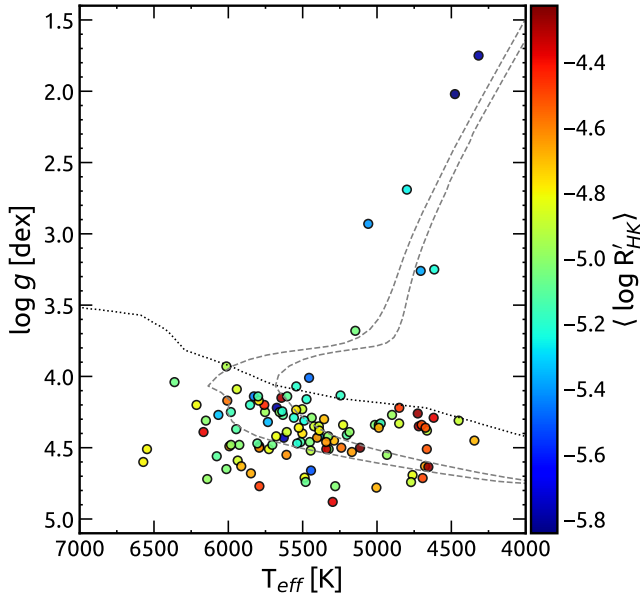


Figure 1. Kiel diagram for the sample stars. The gray dashed lines represent solar metallicity 4.6 and 10 Gyr old stellar evolution tracks from Yonsei-Yale. The colors of the circles indicate stellar activity as measured by the $\log R'_{\text{HK}}$ indicator (Section 4) and corresponding to the color bar. The main sequence stars and the evolved stars are separated by the black dashed line.

their $\log R'_{\text{HK}}$ index (which will be derived in Section 4) as indicated by the color bar. We also show two Yonsei-Yale isochrones (Yi et al. 2001, 2003; Demarque et al. 2004; Han et al. 2009) corresponding to 4.6 and 10 Gyr as dashed gray lines. The majority of the stars in this study are on the main sequence, with a small number of them having lower values of $\log g$ which are indicative of evolved stars. The black dashed line in Figure 1 represents the adopted division between main-sequence and evolved stars. Here we use the same division between main sequence and subgiants and giants that was adopted in Gomes da Silva et al. (2021) which is from Ciardi et al. (2011).

Comparisons of the derived stellar parameters with results from the literature find, in general, reasonable agreement. There is good agreement between our values of T_{eff} s with those from the works of Petigura et al. (2018) and Mayo et al. (2018), as well as the DR17 APOGEE (Majewski et al. 2017) and the DR3 GALAH (Buder et al. 2021) surveys. Comparisons of the different temperature scales find median differences values of T_{eff} (“Other Work” - “This Work”) and MADs (Median Absolute Deviations) of: $+22 \pm 71$ and $+35 \pm 74$ K for the two first studies, and -16 ± 66 and -52 ± 65 K for the two surveys, respectively. The comparison with T_{eff} s from the Gaia survey (Gaia Collaboration et al. 2016,

Table 2. Iron Line List

λ (Å)	Species	χ (eV)	$\log gf$	<i>Sensitive</i>	EW_{\odot} (mÅ)
4088.560	26.0	3.640	-1.720	Y	...
4091.560	26.0	2.830	-2.310	Y	...
4365.896	26.0	2.990	-2.250	N	50.83
4389.245	26.0	0.052	-4.583	Y	...
4445.471	26.0	0.087	-5.441	N	41.07
4485.970	26.0	3.640	-2.530	Y	...
...

NOTE—The complete table is available in machine-readable format. Here, a portion is provided for reference regarding its format and content. Lines with (Y) are sensitive to activity. Lines with (N) are not sensitive. Lines marked with (*) were excluded from the analysis of stellar parameters for all stars because their equivalent widths exceeded 120 mÅ.

2023) and the DR8 LAMOST survey (Cui et al. 2012) reveals slightly more significant systematic differences and MADs of -52 ± 95 and -62 ± 107 K, respectively.

Our values of $\log g$ also generally agree, within the uncertainties, with those from the mentioned works/surveys, with median differences in $\log g$ from ~ -0.02 to 0.02 dex and MAD values from ± 0.13 to ± 0.18 . For Mayo et al. (2018) and LAMOST, however, we find higher systematic differences of $+0.16 \pm 0.12$ and -0.03 ± 0.14 dex, respectively. Finally, our $\log g$ values overall compare well with those based on asteroseismology for K2 stars from Huber et al. (2016): median $\log g$ difference (\pm MAD) of -0.01 ± 0.22 dex. But we note that there are four stars with significant differences, with this work finding them to be dwarfs ($\log g$ varying between 4.3 to 4.8 with uncertainties between 0.08 and 0.2), while Huber et al. (2016) find them to be more evolved ($\log g$ varying between 2.7 to 3.7 with uncertainties from 0.07 to 0.53 dex). These are: EPIC 220481411, EPIC 211413752, EPIC 212012119, and EPIC 212782836, which are nearby stars with distances of approximately 114, 321, 123, and 184 pc, and absolute V -magnitudes of 7.04, 6.39, 6.69, and 5.79, respectively, placing them as K-dwarf stars and more in line with our $\log g$ values. (See also discussion in Section 3.1 of differences in the derived radii with Huber et al. (2016)).

3.1. Stellar Masses & Radii

We calculated the stellar masses and radii using the isochrone method, which involves estimating these fundamental parameters by comparing the positions of stars in a $T_{\text{eff}} - M_V$ diagram with theoretical isochrones. To perform this analysis, we used the PARAM code v1.3 (da Silva et al. 2006) which derives stellar mass, ra-

Table 3. Stellar Parameters

ID	$\langle S_{\text{HK}} \rangle$	σ	$\langle \log R'_{\text{HK}} \rangle$	σ	# Sp	T_{eff}	log g	A(Fe)	ξ	R_{star}	M_{star}	$v \sin i$
						(K)	(dex)	(dex)	(km.s^{-1})	(R_{\odot})	(M_{\odot})	(km.s^{-1})
EPIC211319617	0.166	0.019	-5.024	0.123	15	5281 ± 54	4.77 ± 0.15	6.82 ± 0.03	0.89 ± 0.29	0.674 ± 0.015	0.711 ± 0.018	1.64 (1)
EPIC211331236	2.488	...	-4.648	...	1 \pm NaN	... \pm ...	2.91 (1)
EPIC211342524	0.259	...	-4.571	...	1	6007 ± 163	4.17 ± 0.28	7.08 ± 0.11	2.53 ± 1.64	1.611 ± 0.097	1.031 ± 0.047	7.80 (2)
EPIC211351816	0.110	0.023	-5.374	0.108	7	4706 ± 74	3.26 ± 0.22	7.62 ± 0.07	1.44 ± 0.14	3.699 ± 0.132	1.118 ± 0.079	3.70 (2)
EPIC211355342	0.149	0.017	-5.139	0.138	9	5514 ± 23	4.46 ± 0.06	7.62 ± 0.03	1.02 ± 0.14	1.012 ± 0.020	0.953 ± 0.017	1.63 (1)
...

NOTE—The $v \sin i$ values come from the literature, APOGEE DR17 (1) and [Petigura et al. \(2018\)](#) (2). This table is published in its entirety in the machine readable format. A portion is shown here for guidance regarding its form and content.

dus, luminosity, age, etc., based on a grid of PARSEC isochrones ([Bressan et al. 2012](#)) employing Bayesian inference methodology. The required input parameters are T_{eff} and $[\text{Fe}/\text{H}]$, determined spectroscopically in this work, and the absolute magnitude (M_V) derived using the parallax measurements obtained from Gaia DR3 data ([Gaia Collaboration et al. 2021](#)). In Table 3 are shown the derived masses and radii of the sample stars.

As a comparison, we also determined the stellar radii and masses for the studied stars using the code q^2 (as in [Loaiza-Tacuri et al. \(2023\)](#)), which is based on a grid of Yonsei-Yale isochrones ([Yi et al. 2001, 2003](#)). The results obtained with q^2 are in good agreement with those from PARAM. The median differences “PARAM – q^2 ” are $-0.03 \pm 0.02 R_{\odot}$ for radii and $-0.01 \pm 0.01 M_{\odot}$ for masses.

The distributions of stellar masses and radii for our sample are displayed in Figure 2, revealing that the majority of the sample stars have stellar radii $< 2 R_{\odot}$ and masses $< 1.2 M_{\odot}$. The median radius of the distribution is $0.92 R_{\odot}$ (16th percentile = 0.70; 84th percentile = 1.35) and median mass is $0.92 M_{\odot}$ (16th percentile = 0.74; 84th percentile = 1.05).

The stellar masses and radii obtained here using the isochrone method are compared with results from asteroseismology from [Huber et al. \(2016\)](#) in Figure 3, with stellar radii shown on the left panel and masses on the right panel.

Overall the derived radii and masses compare well with [Huber et al. \(2016\)](#), with a small systematic difference, except for a few clear outliers. The median (\pm MAD) of the differences between the stellar radii from [Huber et al. \(2016\)](#) minus ours is $0.06 \pm 0.12 R_{\odot}$. We note, however, that there seems to be a slight trend for the more evolved stars having radii roughly larger than $\sim 4 R_{\odot}$. Concerning the masses, a small systematic difference is found between our stellar mass determinations and those of [Huber et al. \(2016\)](#) (see right panel Figure

3). Our masses are smaller than those from asteroseismology with a small median (\pm MAD) of the differences of $0.04 \pm 0.06 M_{\odot}$.

One of the outliers in the radius comparison with [Huber et al. \(2016\)](#) is particularly significant - star EPIC 215346008, for which we obtained a stellar radius of $10.141 \pm 0.342 R_{\odot}$ which is about 3 times smaller than the one in [Huber et al. \(2016\)](#) of $36.613 R_{\odot}$, but the latter has an extremely large uncertainty of $+86.878$ and $-8.192 R_{\odot}$. This star is also reported in [Petigura et al. \(2018\)](#) as having $12.34 R_{\odot}$, which is more similar to ours, while in [Hardegree-Ullman et al. \(2020\)](#), who obtained radius from Stefan-Boltzmann law using stellar parameters from the LAMOST survey, this star has $24.224 R_{\odot}$. Finally, we note that in Gaia DR3 the radius for this star is $29.53 R_{\odot}$ with a 68% confidence interval ranging from $28.29 R_{\odot}$ to $30.52 R_{\odot}$, based on the 16th and 84th percentiles, respectively. Another star with a large difference in radius in this comparison is EPIC 220481411, for which we obtain $0.609 \pm 0.012 R_{\odot}$, while [Huber et al. \(2016\)](#) obtain $6.924^{+4.716}_{-2.805} R_{\odot}$. Other results in the literature also find radii in better agreement with our result: [Livingston et al. \(2018, 0.69 \$R_{\odot}\$ \)](#), [Persson et al. \(2018, 0.72 \$R_{\odot}\$ \)](#), [Mayo et al. \(2018, 0.67 \$R_{\odot}\$ \)](#), [Petigura et al. \(2018, 0.71 \$R_{\odot}\$ \)](#), and [Kruse et al. \(2019, 0.64 \$R_{\odot}\$ \)](#). EPIC 220481411 is a nearby star with a well-determined parallax from Gaia DR3 of $\pi=8.69$ mas, with a distance of ~ 115 pc and, with an apparent V -magnitude of 12.48, the absolute V -magnitude is $M_V=7.15$, placing this star squarely in the realm of the K-dwarfs, where a sub-solar radius is expected, giving confidence to our derived radius.

Concerning the mass comparison, the most significant outlier in Figure 3 is the star EPIC 220503133, for which we find $2.021 \pm 0.203 M_{\odot}$, while the asteroseismic result from [Huber et al. \(2016\)](#) is $2.543^{+0.328}_{-0.393} M_{\odot}$, with results overlapping within the error bars.

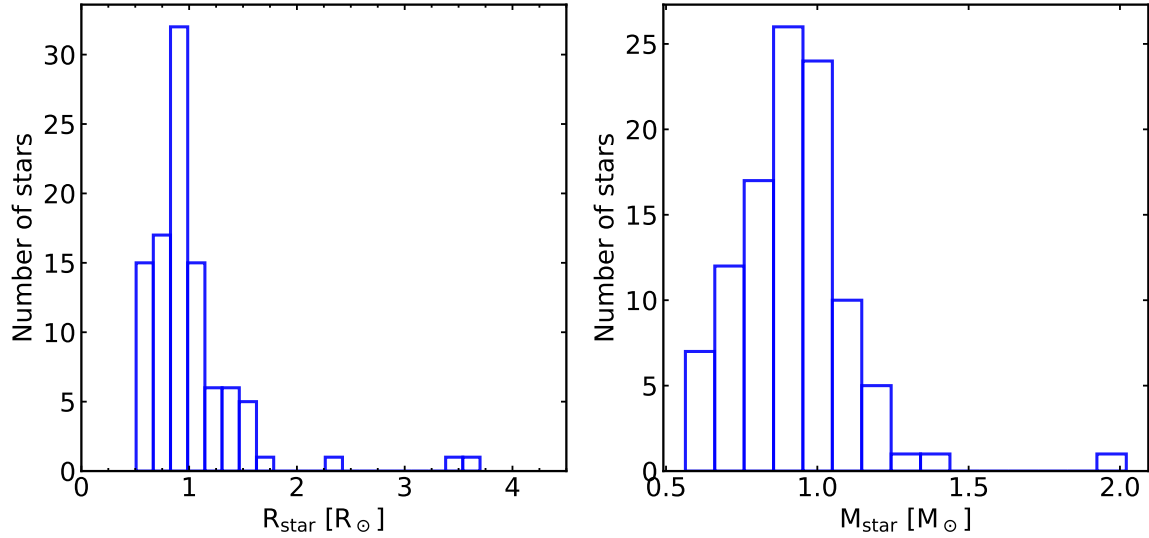


Figure 2. Mass and radius distributions for the sample stars. For better visualization, those few stars in our sample with stellar radii larger than $4 R_{\odot}$ are not shown in the figure.

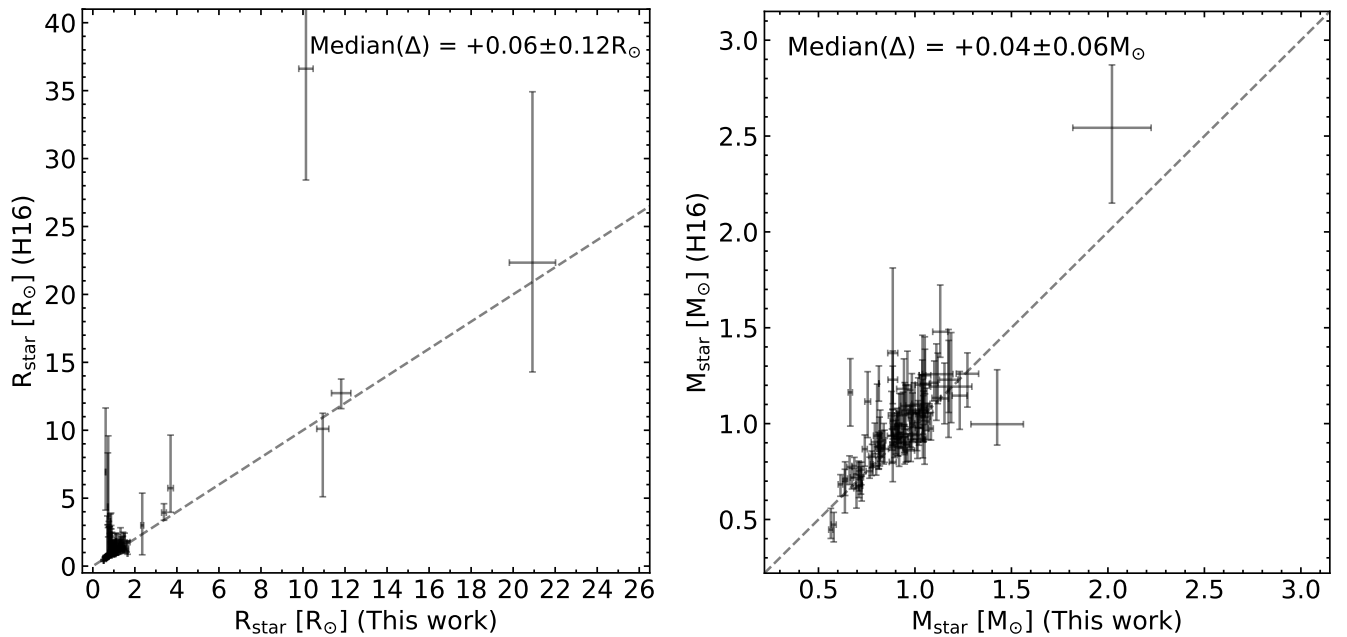


Figure 3. Comparisons of the stellar radii and masses in this study with those determined through asteroseismology by Huber et al. (2016, H16). The median differences (‘Other Work - This Work’) between the parameters and the corresponding MAD are indicated in each case.

3.2. Planetary Radii

The planetary radii were determined using the inferred stellar radii and the transit depth (ΔF), which represents the fraction of stellar flux lost during the planet’s transit minimum, given by Seager & Mallén-Ornelas (2003):

$$R_{pl} = 109.1979 \times \sqrt{\Delta F \times 10^{-6}} \times R_{star}, \quad (1)$$

where the planet’s radius is given in terms of Earth radii.

For our analysis, we considered only the ΔF values of confirmed planets. All candidates or false positives, according to the NASA Exoplanet Archive notes, were excluded from our planet sample. The ΔF values were obtained from Kruse et al. (2019), Barros et al. (2016), Pope et al. (2016), and Christiansen et al. (2017), and these values, along with the star identifications, planet names, planetary radii (R_{pl}) and their corresponding er-

Table 4. Planetary Radii

Star ID	Planet Name	ΔF	R_{pl}	δR_{pl}
		(ppm)	(R_{\oplus})	(R_{\oplus})
EPIC211319617	K2-180 b	1189.0	2.54	0.07
EPIC211351816	K2-97 b	680.0	10.53	0.44
EPIC211355342	K2-181 b	828.0	3.18	0.08
EPIC211399359	K2-371 b	28460.0	12.75	0.03
EPIC211413752	K2-268 b	398.0	1.60	0.08
EPIC211413752	K2-268 c	1239.0	2.82	0.08
EPIC211413752	K2-268 d	531.0	1.84	0.06
EPIC211413752	K2-268 e	436.0	1.67	0.06
EPIC211413752	K2-268 f	1025.0	2.56	0.09
...

NOTE—Transit depth (ΔF) collected from Kruse et al. (2019), Pope et al. (2016), Barros et al. (2016), and Christiansen et al. (2017) for K2 planets. This table is published in its entirety in the machine readable format. A portion is shown here for guidance regarding its form and content.

rors (δR_{pl}), are listed in Table 4. The comparison between the radii of exoplanets orbiting K2 host stars determined here and those in Loaiza-Tacuri et al. (2023), Hardegree-Ullman et al. (2020), Kruse et al. (2019), Petigura et al. (2018), and Mayo et al. (2018) is shown in Figure 4. In general, the median differences in planetary radii (“Other Work – This Work”) are small, varying between ~ -0.13 and $\sim +0.08$; more specifically corresponding to 6% difference for Kruse et al. (2019), 7.6% for Hardegree-Ullman et al. (2020), 10.7% for (Petigura et al. 2018), 11.1% for Mayo et al. (2018), and 1.3% for Loaiza-Tacuri et al. (2023).

3.2.1. Planetary Radii and the Radius Gap

Figure 5 shows the distribution of planetary radii for our sample of 93 confirmed planets orbiting 69 K2 stars. Not unexpectedly, there is a dearth of planets around $R_{gap} \sim 1.9 R_{\oplus}$ for the smaller planets in the sample ($R_{pl} < 4 R_{\oplus}$). Similarly to what was found in our previous study of K2 targets based on Hydra spectra (Loaiza-Tacuri et al. 2023) and with a similar number of confirmed planets, our methodology for determining stellar radii and, from them, planetary radii allowed for the identification of the radius gap, also known as the Fulton gap (Fulton et al. 2017). This well known feature has been widely confirmed in various studies using the Kepler sample (Berger et al. 2018; Fulton & Petigura 2018; Van Eylen et al. 2018; Martinez et al. 2019) and the fact that our results depict the gap attests to the high quality and precision achieved by our spectroscopic analysis. The error budget in the derived radii are discussed in the section below.

Table 5. Error budget

Parameter	Median Uncertainty
T_{eff}	42 K
$\log g$	0.09 dex
A(Fe)	0.03 dex
V	0.04 mag
plx	0.02 mas
M_{star}	0.02 M_{\odot}
R_{star}	1.79%
ΔF	2.79%
R_{pl}	2.33%

3.3. Uncertainties in the Derived Parameters

The formal errors adopted for the stellar parameters T_{eff} , $\log g$, and ξ were computed using q^2 , which follows the error analysis discussed in Epstein et al. (2010) and Bensby et al. (2014). Errors in the iron abundances, A(Fe I) and A(Fe II), were obtained by combining errors estimated from the equivalent-width measurements with stellar parameter uncertainties. The individual errors of these parameters are presented in Table 3.

The median errors in the stellar parameters derived in this study are reported in Table 5: $\delta T_{eff} = 42$ K, $\delta \log g = 0.09$ dex, $\delta A(\text{Fe}) = 0.03$ dex, and $\delta \xi = 0.17$ km.s^{-1} . Following a similar approach to that employed by Loaiza-Tacuri et al. (2023), we have taken into account the contributions of individual errors in determining the error budget for derived parameters, such as M_{star} , R_{star} , and R_{pl} . It is important to note that the error in the V magnitude contributes about 0.15% to the error in the stellar radius, assuming a median error of 0.04 mag for the V magnitudes of our stars. In addition, errors in parallaxes, with a median error of 0.02 mas, result in a 0.66% error in both stellar mass and radius. The uncertainties in stellar radii and transit depth errors (ΔF) have a direct influence on the determination of planetary radius errors. The median internal uncertainty in our derived stellar radius distribution is 1.8%. For the transit depth values (ΔF) and their associated errors, we adopted data from Kruse et al. (2019), Barros et al. (2016), and Christiansen et al. (2017), resulting in an internal transit depth precision of 2.8% for the planets in our sample. Ultimately, these combined uncertainties contribute to an internal precision of 2.3% in the error budget for the radius of the planets (R_{pl}). Table 5 summarizes the error budgets for our R_{star} and R_{pl} determinations.

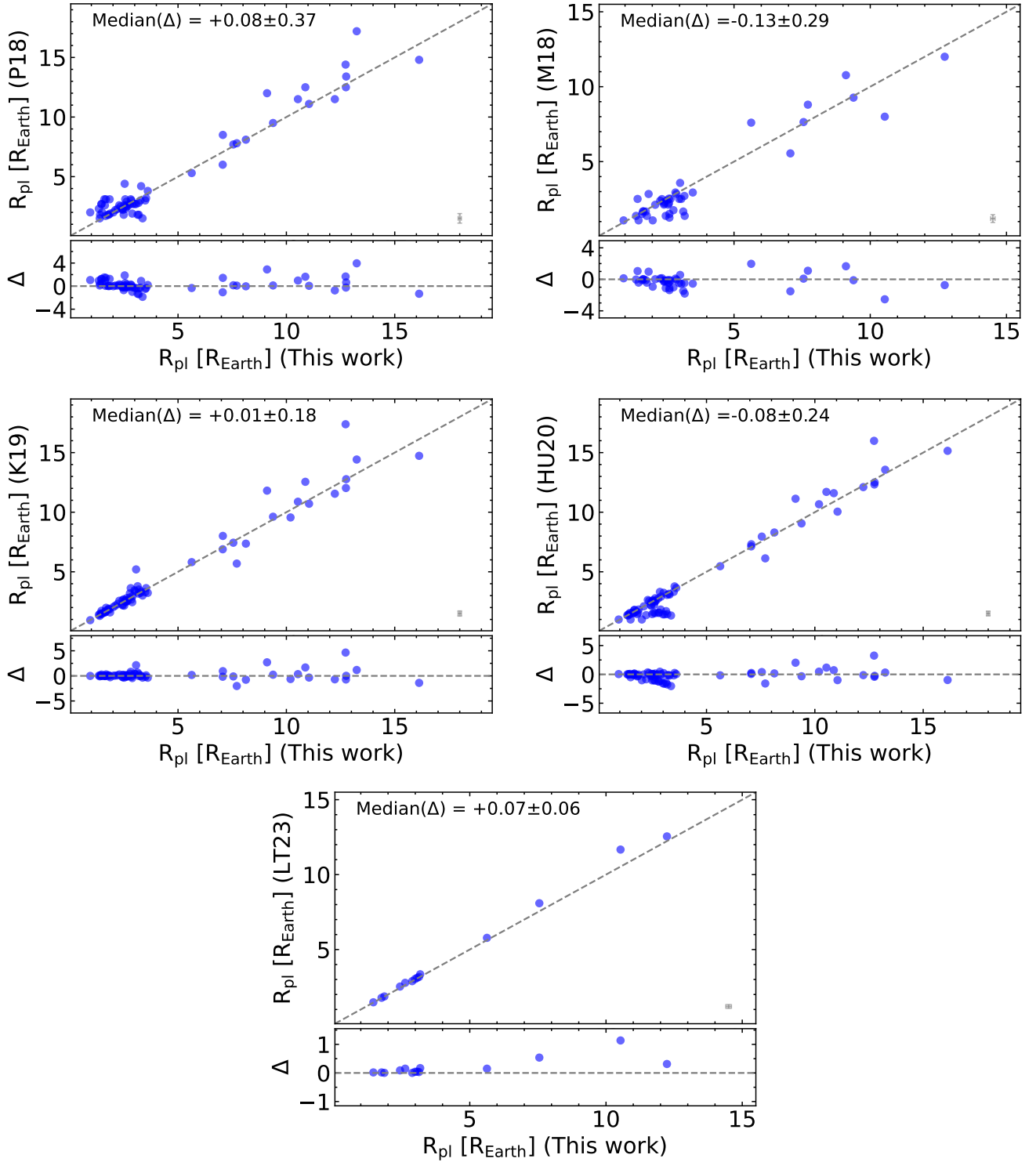


Figure 4. Comparisons of the planetary radii in this study with those from Petigura et al. (2018, P18.), Mayo et al. (2018, M18), Kruse et al. (2019, K19), Hardegree-Ullman et al. (2020, HU20), and Loaiza-Tacuri et al. (2023, LT23). The bottom sub-panels show the difference between ‘Other Work - This Work’ (Δ). The median differences between the parameters and the corresponding MAD are indicated in each case. The black dashed lines represent equality.

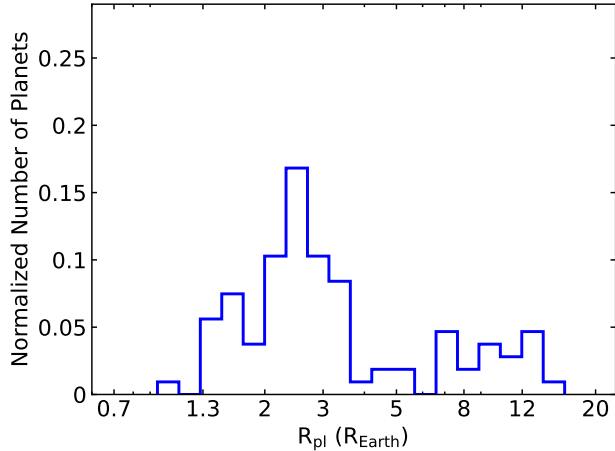


Figure 5. The planetary radius distribution for the K2 planet sample. The location of the gap in the planetary radius distributions is approximately at $R_{\text{gap}} \sim 1.9 R_{\oplus}$.

4. MEASUREMENTS OF THE CALCIUM H AND K LINES

The Ca II H and K lines are useful diagnostics of chromospheric activity due to the sensitivity of their line cores to chromospheric temperature inversions, which are related to magnetic activity (Leighton 1959). Quantitative Ca II H and K activity levels can be expressed using the S-index, also known as the Mount Wilson index (Vaughan et al. 1978, S_{MW}). The S-index is defined as a ratio of fluxes measured in the H and K line cores and fluxes in nearby pseudo-continuum passbands, which are labeled R and V. In this study these fluxes were measured following the procedure described in Isaacson & Fischer (2010) and using the IRAF⁵ task `sbands`. Fluxes in the H and K line cores were measured using a triangular bandpasses (full width at half maximum of 1.09 Å) centered at $\lambda 3968.47$ Å and $\lambda 3933.67$ Å, respectively, while the pseudo-continuum R and V fluxes were measured using rectangular bandpasses of 20 Å, centered at $\lambda 3901$ Å and $\lambda 4001$ Å, respectively.

Isaacson & Fischer (2010) provide a defining equation for the S_{HK} -index from HIRES spectra of

$$S_{HK} = 32.510 \frac{(H + 1.45K)}{(R + 25V)} + 0.021 \quad (2)$$

where the coefficient for V was set in order to bring the mean fluxes in the R and V continuum bandpasses to approximately the same levels. Our use of this equation

led to unrealistically small values of S_{HK} for our HIRES spectra. Following the discussion in Isaacson & Fischer (2010), we investigated what V-coefficient would bring the measured R and V mean-fluxes to approximately the same levels in our HIRES spectra (see Figure 6), and found a mean V-coefficient from all spectra of 2.28, with a small scatter. The computation of S_{HK} used a unique V-coefficient for each spectrum such that the R and V mean fluxes were equal.

We measured the S_{HK} index in a total of 725 spectra from 144 K2 stars, noting that for 40 of our targets there were two or more spectra available in the Keck Archive, with the other stars having only one HIRES observation. The measured S_{HK} index for the stars are presented in Table 3, noting that for those stars having more than one observation, the values in the table are the mean (and standard deviation) of the S_{HK} measurements. The S_{HK} indices for our K2 sample will be discussed in Section 5 and validated from comparisons with the literature below.

We opted to place our S_{HK} measurements from archival spectra onto the commonly used Mt. Wilson scale via a comparison for stars in common with the following studies, all of which have transformed their respective S_{HK} values onto the Mt. Wilson scale: Chahal et al. (2023), who used LAMOST spectra, Brown et al. (2022), who used spectra from NARVAL and ESPaDOnS, Gomes da Silva et al. (2021), Mayo et al. (2018), and Isaacson & Fischer (2010) who used spectra from HARPS, TRES, and HIRES, respectively. The comparisons are shown in Figure 7, with the largest number of stars in common being Chahal et al. (2023), where the median of the differences (and MAD) between S_{HK} (“Chahal - This Work”) are -0.033 ± 0.052 , respectively. These are small differences and the overall comparisons with Chahal et al. (2023), as well as for the other studies, are good. The solid red line in Figure 7 is the least squares fit of $S_{HK}(\text{This Work})$ as a function of $S_{HK}(\text{Other})$, while the dashed line is a one-to-one line. The fitted slope of $m=1.10$ and the intercept of $b=0.00$ results in differences between the fitted line and the one-to-one line that are so small we chose not to apply any transformation to our S_{HK} measurements. This close correspondence with the Mt. Wilson scale also indicates that the equation given in Isaacson & Fischer (2010), with a V-flux coefficient adjusted to the values for each spectrum, yields values of S_{HK} that are close to the Mt. Wilson system. We note that the star highlighted in parentheses in Figure 7 (EPIC 212069861) is a M0-dwarf, one of the most active stars in our sample. The S_{HK} measurement for this star in this study was derived from a single available Keck HIRES spec-

⁵ Image Reduction and Analysis Facility (IRAF) is distributed by the National Optical Astronomy Observatory, which is operated by the Association of Universities for Research in Astronomy, Inc., under a cooperative agreement with the National Science Foundation.

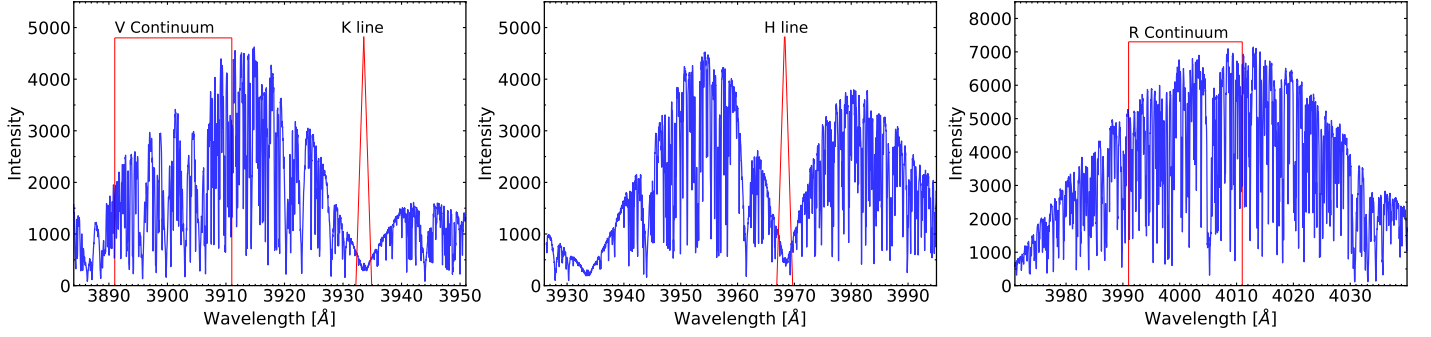


Figure 6. Keck HIRES spectra of the star EPIC220383386 showing the three echelle orders containing the calcium H and K lines and pseudo-continuum at V and R.

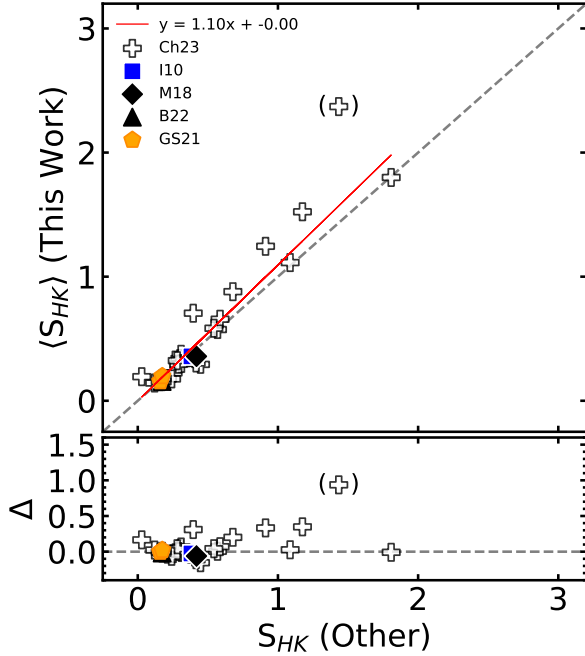


Figure 7. Comparison of the derived S-indices for stars in common with other studies in the literature. The crosses correspond to Chahal et al. (2023, Ch23), open circles to Zhang et al. (2022, Z22), triangles to Brown et al. (2022, B22), pentagon to Gomes da Silva et al. (2021, GS21), diamond to Mayo et al. (2018, M18), and square to Isaacson & Fischer (2010, I10). The gray dashed line in the upper panel represents equality, while the red solid line represents the best fit between our results and the literature.

trum observed on November 11, 2016. Given the very large difference in the S_{HK} measurements for this star, it is likely that its activity level has varied significantly between the measurements here ($S_{HK} = 2.37$) and in Chahal et al. (2023) ($S_{HK} = 1.43 \pm 0.08$). This star has not been included in the best fit slope shown in Figure 7.

4.1. Conversion from S-index to R'_{HK}

The equation for the S-index includes terms with flux contributions from both the chromosphere plus the basal photosphere, which are referred to as R'_{HK} and R_{phot} , respectively. In order to isolate and measure chromospheric activity in stars with different effective temperatures, it is necessary to subtract the photospheric contribution by considering the dependence of the R and V fluxes on the effective temperature. We adopted the method described in Noyes et al. (1984), taking

$$R'_{HK} = R_{HK} - R_{phot} = 1.34 \times 10^{-4} C_{cf} S_{HK} - R_{phot}, \quad (3)$$

where the photospheric contribution, R_{phot} , and the temperature dependent bolometric correction factor, C_{cf} , are modeled as polynomial functions of $(B - V)$:

$$\log R_{phot} = -4.898 + 1.918(B - V)^2 - 2.893(B - V)^3. \quad (4)$$

Since our sample includes FGK dwarfs and some evolved stars, we applied the bolometric corrections proposed by Rutten (1984), defined for $0.3 \leq (B - V) \leq 1.7$.

For main sequence stars, taken as those stars falling below the black dashed line in Figure 1, we used:

$$\log C_{cf} = 0.25(B - V)^3 - 1.33(B - V)^2 + 0.43(B - V) + 0.24, \quad (5)$$

while for evolved stars we used:

$$\log C_{cf} = -0.066(B - V)^3 - 0.25(B - V)^2 - 0.49(B - V) + 0.45. \quad (6)$$

Finally, R'_{HK} in Equation 3 depends only on $(B - V)$, and the applicability of this relations is no longer limited only to late-F to early-K dwarfs. The mean $\log R'_{HK}$ obtained for our sample stars are presented in Table 3.

5. DISCUSSION

5.1. Stellar Activity of the Sample K2 Targets

In Section 4 we discussed the derivation of the S_{HK} index, and in the left panel of Figure 8 we show the distribution of the derived indices for our sample of K2

stars. Most of the K2 targets in this study have $S_{\text{HK}} < 0.2$, with the median of the distribution of $S_{\text{HK}} = 0.178$ (16th percentile 0.134; 84th percentile = 0.577). There are, however, a few stars in our sample that have $S_{\text{HK}} \sim 2 - 3$, signifying high levels of activity. The range of S_{HK} -index values measured in this sample are similar to those presented in the large compilation of Mt. Wilson measurements from Duncan et al. (1991). In the right panel of Figure 8 we show the S_{HK} index distribution obtained for the star in our sample having the largest number of available HIRES spectra, EPIC 220725186. The S_{HK} -index determinations for this star were based on 211 HIRES spectra collected over a period of six years (from July 10 2016 to January 19, 2022). The distribution of the S_{HK} indices for this star is peaked, having a mean S_{HK} -index of 0.154 ± 0.021 (median of 0.158 ± 0.009), which indicates small stellar variability and its mean S_{HK} -index is similar to the peak of the S_{HK} -index distribution of our K2 sample.

It is useful for our discussion to note the S-index of the Sun within the distribution of S_{HK} -index values shown in the left panel of Figure 8. Egeland et al. (2017) used solar observations from both Mt. Wilson and Sacramento Peak to place the Sun on the Mt. Wilson S_{HK} -index scale. Over solar cycles 15-24, Egeland et al. (2017) find a mean S-index of $\langle S \rangle = 0.1694 \pm 0.0020$, and at solar minima (the quiet Sun) to be $\langle S_{\text{min}} \rangle = 0.1621 \pm 0.0008$. The variations in the S-index over the solar cycle were found to have a mean full amplitude of $\langle \Delta S_{\text{cyc}} \rangle = 0.0145 \pm 0.0012$. Lorenzo-Oliveira et al. (2018) used ESO/HARPS spectra to measure the solar S-index from reflected light of solar system objects, in the same Mount-Wilson scale as that used for their sample of solar twins observed through the same spectrograph, and found an average solar activity of $\langle S_{\text{MW}} \rangle = 0.17$. Using a correlation between activity and sunspots, they estimated an average S-index for the solar cycles 15 - 24 of $\langle S_{\text{MW}} \rangle = 0.1696 \pm 0.0025$, in perfect agreement with the same cycles analyzed by (Egeland et al. 2017). Since most of the stars in our sample have only one, or a few observations, our S_{HK} measurements present a “snapshot” of chromospheric activity over the sample of stars which were caught in random phases over their respective activity cycles and, thus, we are not in a position to discuss individual stellar magnetic cycles nor rotational period coverage. Nonetheless, our results yield a distribution of S_{HK} values sampled at random over a population of FGK stars and we now discuss some characteristics of this sample.

5.1.1. S_{HK} vs. $(B - V)$

Figure 9 shows the S_{HK} for the K2 targets measured here as a function of their $(B - V)_0$ color. Both Isaacson & Fischer (2010) and Boro Saikia et al. (2018) observed an increase in the S-index for $(B - V)$ colors ranging from ~ 1.0 to 1.4 in a sample of ~ 2600 and ~ 4400 main-sequence stars, respectively. The lower envelope increase of S_{HK} with increasing $(B - V)_0$ is due primarily to the decreasing flux in the V and R continuum fluxes in cooler stars relative to the fluxes in the Ca II H and K lines (e.g., Isaacson & Fischer 2010). In this study of 144 K2 stars within the same range in $(B - V)_0$, our results for S-index vs $(B - V)_0$ shown in the figure also exhibit a similar pattern for $(B - V) < 1.4$, as the S-index begins to increase roughly at $(B - V)_0 \sim 0.8$. The general agreement is made clearer in comparison with the orange dashed line in the figure, which represents the polynomial fit, taken from Isaacson & Fischer (2010), and traces the lower envelope of their distribution.

In our sample the lower activity limit remains approximately constant for $(B - V)_0 \lesssim 0.9$, while for redder colors in the range of $0.9 \lesssim (B - V)_0 \lesssim 1.4$, the lower limit of the S-index exhibits a smooth increase, from $S_{\text{HK}} \sim 0.2$ at $(B - V)_0 = 0.9$ up to $S_{\text{HK}} \sim 0.8$ at $(B - V)_0 = 1.4$, and begins to decrease for $(B - V)_0 \gtrsim 1.4$. Notably, throughout this entire range, the highest levels of activity, or the fraction of active stars, increase sharply towards redder values of $(B - V)_0$ (later spectral types). For colors of $(B - V)_0 < 0.9$ there are only 8 stars out of 30 stars with $S_{\text{HK}} > 0.4$ (roughly twice the value of the lower envelope), while in the range of $(B - V)_0 \sim 0.9$ to 1.2 there are 14 stars out of 22 that exhibit S_{HK} values that are more than twice the lower envelope.

5.1.2. R'_{HK} and Stellar Rotation

As a star evolves it loses angular momentum, resulting in lower stellar rotational velocities, which is accompanied by a decrease in stellar activity (Skumanich 1972). In order to analyze the behavior of the activity index R'_{HK} in relation to $v \sin i$ and stellar rotational period, we collected $v \sin i$ measurements for our sample stars from the DR17 APOGEE survey (Majewski et al. 2017) and Petigura et al. (2018), these values are presented in the last column of the Table 3. The $v \sin i$ sample is a mixture of Keck/HIRES spectra, with $R \sim 60,000$, and APOGEE spectra, with $R \sim 22,400$, providing theoretical lower limits to $v \sin i$ detections of roughly $\sim 2 - 3$ km-s $^{-1}$. The rotational periods for the sample were taken from Reinhold & Hekker (2020), de Leon et al. (2021), and Rampalli et al. (2021), however rotational periods were available for only 44 sample stars. In Figure 10 we plot $v \sin i$ versus rotational period for those stars that have both measurements available, using dif-

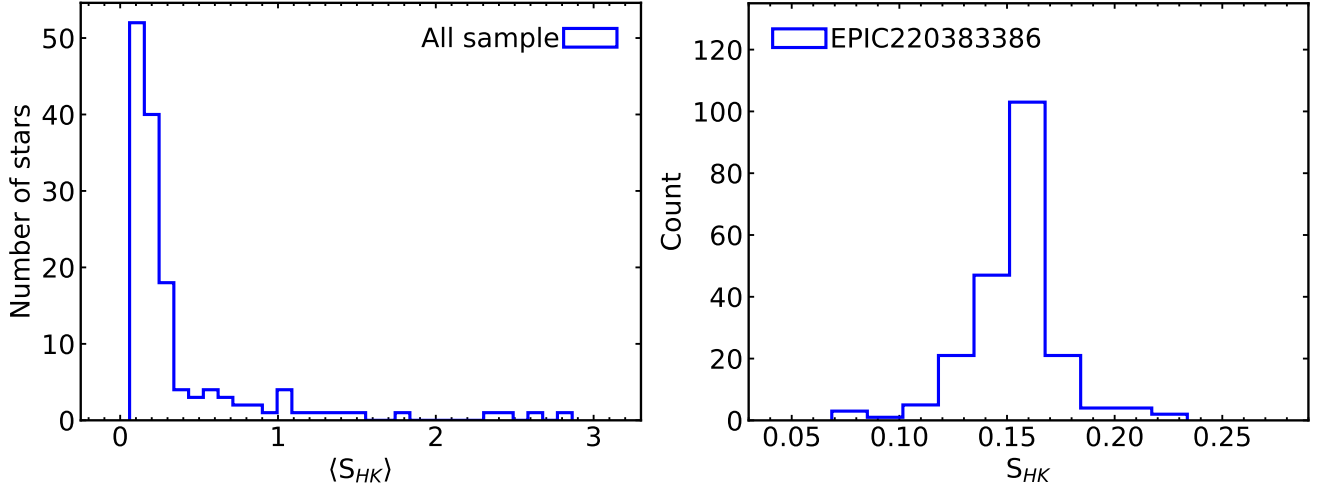


Figure 8. Left panel: the distribution of the mean S_{HK} ($\langle S_{\text{HK}} \rangle$) obtained for 111 K2 stars in our sample. Right panel: the S_{HK} index distribution for the star EPIC 220383386; this is the star in our sample with the largest number of HIRES spectra available: 211 spectra between July 10, 2016, and January 19, 2022.

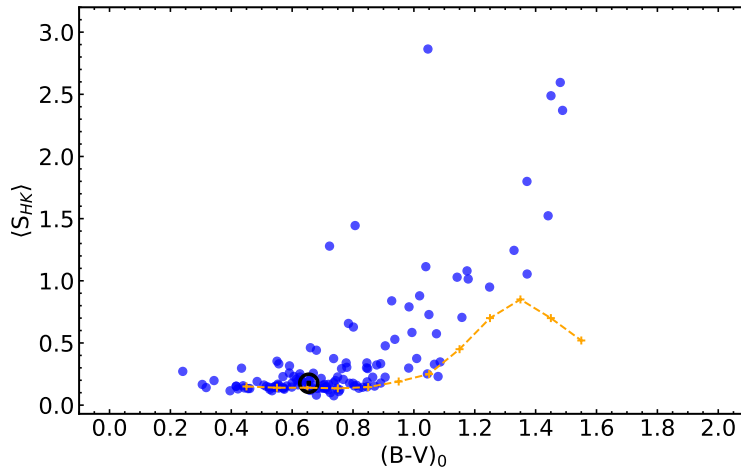


Figure 9. Mean S_{HK} indices as a function of the $(B - V)_0$ color for the main sequence stars in our K2 sample. The solar symbol represents the solar value at $\langle S_{\text{HK}} \rangle = 0.176$ (Mamajek & Hillenbrand 2008), lying close to the dashed orange line taken from Isaacson & Fischer (2010).

ferent symbols for stars as a function of their spectral types and also identify the $v \sin i$ measurement source as either from APOGEE or Petigura et al. (2018). There is an expected increase in $v \sin i$ as the rotational period decreases and the star having the highest $v \sin i$ in this sample ($v \sin i = 13.6 \text{ km/s}$) has a measured rotational period of less than 5 days. These independent measurements are self-consistent: a G-dwarf having an approximate radius of $1 R_{\odot}$ and a rotational period of ~ 4.5 days would have an equatorial rotational velocity of $\sim 12 \text{ km-s}^{-1}$. The behavior of the equatorial rotational velocity as a function of rotational period for $0.5 R_{\odot}$, $1.0 R_{\odot}$, and $1.2 R_{\odot}$ is shown in Figure 10 as the blue, orange and green dashed line, respectively. We can

identify a floor in the $v \sin i$ at around $2\text{--}3 \text{ km-s}^{-1}$ which is likely due to the loss in sensitivity given the intrinsic broadening in stellar spectra due to microturbulence and macroturbulence.

The top left panel of Figure 11 shows $\langle \log R'_{\text{HK}} \rangle$ versus the rotational period for the 44 stars in our sample with measured rotational periods available in the literature, as discussed earlier in this section. The distribution of stars with measured rotational periods for our sample is skewed towards higher levels of activity, with only two stars having $\langle \log R'_{\text{HK}} \rangle < -5.10$. This is likely due to more active stars having stellar surface features, such as spots, that can be detected via K2 photometry. Nevertheless, there is a trend in this sub-sample,

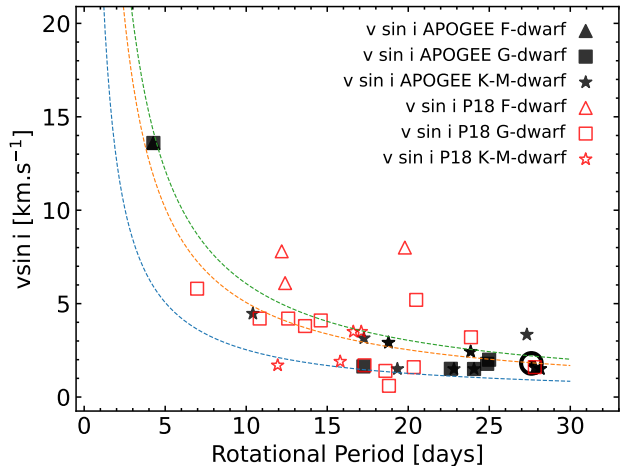


Figure 10. Projected rotation velocities ($v \sin i$) and measured rotation periods for those stars in our sample having the two measurements available in the literature. The different symbols segregate the stars according to their spectral types. The three dashed lines represent the equatorial rotational velocity as a function of rotational period between 0.1 to 30 days, for the following stellar radii: $0.5 R_{\odot}$ (blue), $1.0 R_{\odot}$ (orange), and $1.2 R_{\odot}$ (green).

as illustrated by the red running median and black running mean lines, in which the distribution of $\langle \log R'_{\text{HK}} \rangle$ values remains nearly flat at longer rotational periods ($P \sim 14 - 30$ days) and then increases for lower rotational periods (higher rotational velocities). Our results agree well with measurements of $\langle \log R'_{\text{HK}} \rangle$ versus rotational period for a sample of planet-hosting stars in the Kepler prime field by Morris et al. (2017). As a reference, a period of 12 days for a solar-radius star would have an equatorial rotational velocity of $\sim 4 - 5 \text{ km}\cdot\text{s}^{-1}$.

To further investigate trends between rotation and activity, we derived $P/\sin i$ from the $v \sin i$ values and these are shown in the top right panel of Figure 11, noting that those stars with measured rotational periods have been excluded from this figure. The stars with very large values of $P/\sin i > 80$ days are evolved stars (see Figure 1), with the main sequence stars having $P/\sin i \lesssim 40$ days, keeping in mind that these periods are upper limits, with typical expected inclination effects of $\sim 0 - 40\%$ for half of the sample. Unlike the upper left panel of this figure, with measured photometric periods, this sample exhibits the full range of activity levels and with large scatter in $\log R'_{\text{HK}}$ at a given value of $P/\sin i$. Within this scatter, however, both the lower and upper envelopes define increasing $\log R'_{\text{HK}}$ with decreasing $P/\sin i$ and the points from the upper left panel are contained within the high activity region of the envelope. Although there is not a simple relation in the upper panels of Figure 11, the general trend is that stars show more activity for low

values of $P/\sin i$ with a steep rise in $\langle \log R'_{\text{HK}} \rangle$ beginning at approximately $P/\sin i \sim 30 - 40$ days. The stars with $P/\sin i$ higher than this threshold all show very low levels of activity at $\log R'_{\text{HK}} \sim -5.5$. The lack of a simple relation between $\log R'_{\text{HK}}$ as a function P_{rot} is also found by Böhm-Vitense (2007) in a study of 25 G and K dwarfs which display large scatter in $\log R'_{\text{HK}}$ at a given rotational period, with the suggestion of two sequences that Böhm-Vitense (2007) labels as active (A) and inactive (I), although some stars are found in-between the two sequences. Similar results are found by Metcalfe & van Saders (2017) in a sample of ~ 50 FGK dwarfs. The results from both Böhm-Vitense (2007) and Metcalfe & van Saders (2017) overlap closely our results as presented in the top panels of Figure 11, over the rotational period range of $\sim 5 - 45$ days. To better illustrate this comparison, the approximate envelope in $\log R'_{\text{HK}}$ versus P_{rot} found by Metcalfe & van Saders (2017) in their Figure 2 is outlined by the solid lines in the top right panel of Figure 11, while the dashed lines follow the respective Inactive and Active sequences from Böhm-Vitense (2007) in her Figure 8. These two earlier studies, along with the results presented here, point to a complex interplay between stellar rotational period and chromospheric activity that is likely a function of both stellar mass and age.

The bottom panels of Figure 11 present the literature $v \sin i$ measurements along with their corresponding $\log R'_{\text{HK}}$ values derived in this study, with the left panel showing all stars, while the right panel has an expanded scale showing $v \sin i$ values up to $20 \text{ km}\cdot\text{s}^{-1}$. Given that the $v \sin i$ values represent lower limits to the true rotational velocities, stars with low values of $v \sin i < 3 \text{ km}\cdot\text{s}^{-1}$ (the approximate floor in detection limit from Figure 10) are composed of a mixture of slowly rotating stars and rapidly rotating stars that are viewed at small inclination angles. Stars with higher values of $v \sin i$ can be considered as bone fide rapid rotators. As shown in the right bottom panel of Figure 11, the stars with $v \sin i < 3 \text{ km}\cdot\text{s}^{-1}$, which are a mixture of slow and rapid rotators, exhibit a large range in $\log R'_{\text{HK}}$ and contain 20 stars having high activity levels of $\log R'_{\text{HK}} \geq -4.75$, or 14.3% being in the high activity group. As discussed above, it is likely that a fraction of the stars in this sub-sample are fast rotators viewed at small inclination angles. There remain five stars with $v \sin i > 10 \text{ km}\cdot\text{s}^{-1}$ and this sub-sample rapid rotators contains a larger fraction of 83% (5 out of 6) active stars, with $\log R'_{\text{HK}} \geq -4.75$, supporting the general result that rapidly rotating stars tend to have higher levels of chromospheric activity.

5.1.3. The Vaughan-Preston gap

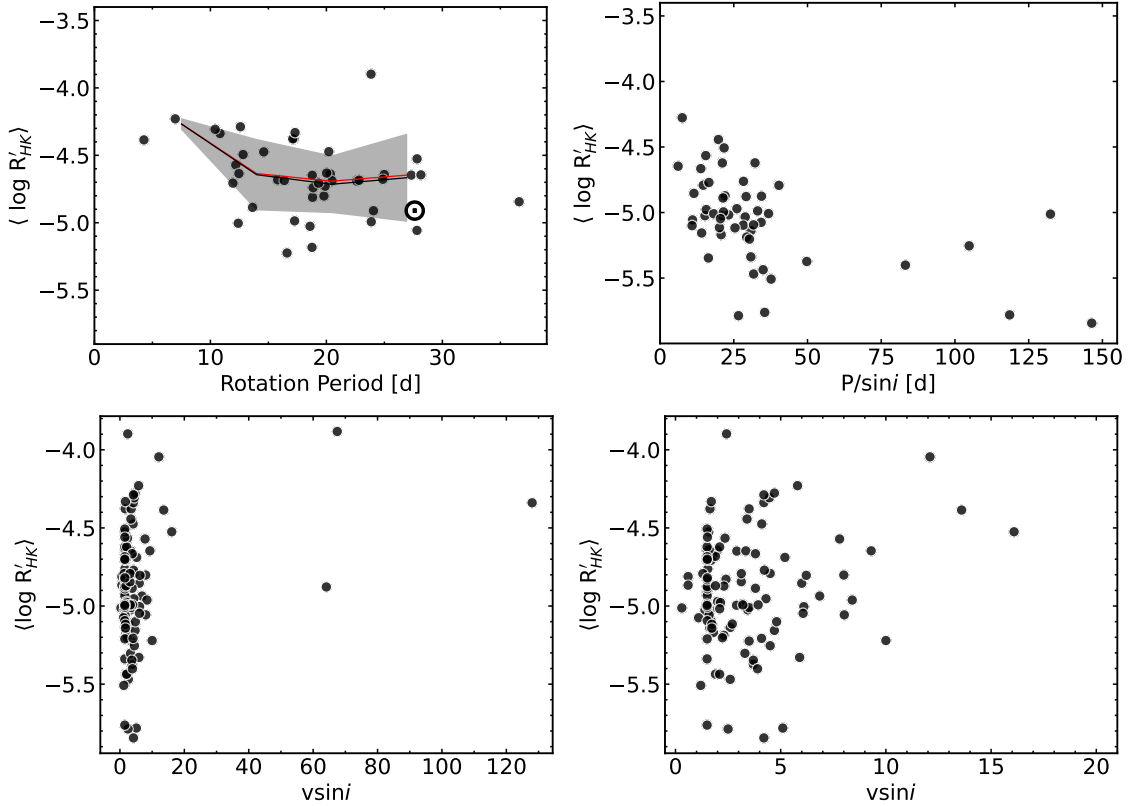


Figure 11. Top right panel: Top right panel shows mean $\log R'_{\text{HK}}$ index as a function of rotational period. The red line represents the running median and the black line the running mean, the gray area is the standard deviation. Bottom panels: mean $\log R'_{\text{HK}}$ index as a function of rotational projected velocity ($v \sin i$).

Vaughan & Preston (1980) used the Ca II H and K lines to map chromospheric activity in 486 field stars in the solar neighborhood as part of the Mount Wilson project (Wilson 1968; Duncan et al. 1991; Baliunas et al. 1995). They found that in this sample there was a lack of F- and G-type stars with intermediate activity levels, which has been labeled the “Vaughan-Preston gap”, with this gap spanning a range in $(B - V)_0$ roughly between 0.4 and 1.1 and values of S_{HK} between 0.2 to 0.7. A lack of stars in this regime was later confirmed by Henry et al. (1996) from an analysis of 800 stars observed with the Coude’ spectrograph on the 1.5 m Telescope at CTIO and more recently by Gomes da Silva et al. (2021) from analysis of HARPS spectra of 1674 FGK stars. Boro Saikia et al. (2018) also investigated stellar activity in a large sample of cool stars using results collected from various surveys in the literature and concluded that the Vaughan-Preston gap may not be a significant feature.

The top panel of Figure 12 shows the distribution of the mean values of $\log R'_{\text{HK}}$ for our sample of main sequence stars and reveals a gap, or valley, with a depth of $\sim 35\%$ of the main peak, at the approximate location of the Vaughan-Preston gap (shown as the vertical

lines), with boundaries as defined in Boro Saikia et al. (2018). This boundary delineates a bimodal distribution around the gap. In the middle panel of the figure we show the $\log R'_{\text{HK}}$ distribution only for the sub-sample of F and G-type dwarfs, using for this selection a threshold of $T_{\text{eff}} > 5000$ K. Although this distribution is not clearly bimodal, it is noted that the peak at the side of the gap corresponding to active stars is smaller when compared to the distribution shown in the top panel of Figure 12. Gomes da Silva et al. (2021) noted bimodal distributions in the values of $\log R'_{\text{HK}}$ for their sample of F and G dwarfs with means close to -4.95 and -4.50 for the inactive and active stars, respectively, which are close to ours. That study, with a much larger number of stars, found overall a similar distribution to ours, with a similarly smaller peak on the active side of the gap when compared to the non-active side. Since Gomes da Silva et al. (2021) had a much larger sample than the one we present here, they carried out two, three, four, and five component Gaussian fits to their results, finding that three and four component models yield somewhat better fits to their results; our sample is not large enough to meaningfully conduct such tests. Gomes da Silva et al. (2021) also found that the K-dwarfs in their

sample had a different distribution of $\log R'_{\text{HK}}$ than the F and G dwarfs and exhibited three distinct peaks, with no Vaughan-Preston gap. Although our sample is dominated by F and G dwarfs, having only 26 K dwarfs, in the bottom panel of Figure 12 we present the $\log R'_{\text{HK}}$ distribution of the K dwarfs. Given the small number of stars in this sub-sample it is hard to conclude that we also see three peaks in the distribution of K dwarfs, although the region of the Vaughan-Preston gap shows a reduced number of stars with the obvious caveat that we have very few K-dwarfs in our sample. One feature of the distribution of these stars is that they all have $\log R'_{\text{HK}} > -5$, none of them belonging to the “very inactive stars” category.

5.1.4. The Impact of Including Activity Sensitive Lines in the Analysis

In Section 3 we described our derivation of stellar parameters that is based upon Fe I and Fe II lines and which relied only on lines deemed to be insensitive to stellar magnetic activity, as described in Yana Galarza et al. (2019). In this section we investigate possible differences between the stellar parameters derived without using activity-sensitive Fe lines (see Section 3) when compared to those derived with the inclusion of a significant number of activity-sensitive Fe lines and check whether any differences in ΔT_{eff} , $\Delta[\text{Fe}/\text{H}]$, or $\Delta\xi$ correlate with $\log R'_{\text{HK}}$. A number of recent studies using high-resolution spectra ($R \sim 115,000$), such as those by Flores et al. (2016), Lorenzo-Oliveira et al. (2018), Yana Galarza et al. (2019), and Spina et al. (2020), have shown that stellar magnetic activity can affect determinations of T_{eff} , ξ , and $[\text{Fe}/\text{H}]$ that are based upon an analysis using Fe I and Fe II lines. Figures 3 and 4 in Spina et al. (2020) show that there can be an enhancement in the strengths of certain magnetically sensitive Fe I lines in stars with $\log R'_{\text{HK}} > -5.0$. As reported by Spina et al. (2020), the presence of stellar activity may lead to differences in the derived effective temperature, metallicity, and microturbulent velocity, but with no significant variations in the surface gravity determinations. In particular, they found a decrease in the effective temperatures for stars with $\log R'_{\text{HK}} > -4.6$, while a decrease in $[\text{Fe}/\text{H}]$ values begins at $\log R'_{\text{HK}} \sim -5.0$, along with an increase in the microturbulent velocity. In addition, Yana Galarza et al. (2019) analyzed several observations of the solar twin star HIP 36515 and showed that the difference in the derived parameters computed with and without activity-sensitive lines varies depending on the phase of the stellar activity cycle. Here we will investigate the impact in the stellar parameter determinations from inclusion of an additional 49 Fe I lines

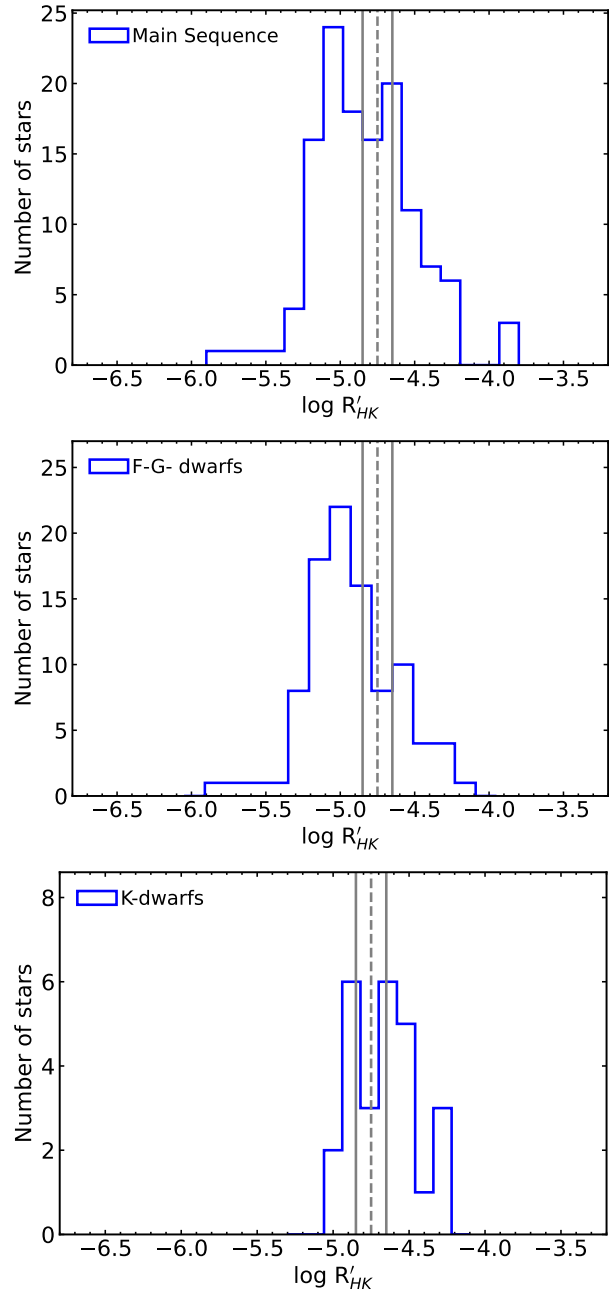


Figure 12. Top panel: the distribution of $\log R'_{\text{HK}}$ for the main sequence stars in our K2 sample. Middle panel: the distribution of $\log R'_{\text{HK}}$ for the F-G- type dwarfs in our sample. Bottom panel: the distribution of $\log R'_{\text{HK}}$ for the K-type dwarfs in our sample. The region of the Vaughan-Preston gap is marked by the gray solid lines in all panels.

and 2 Fe II lines that were found to be sensitive to stellar activity.

As shown in Figure 13 there are systematic differences between the results in the sense that the effective temperatures and metallicities derived including activity sensitive Fe lines are overall larger than those

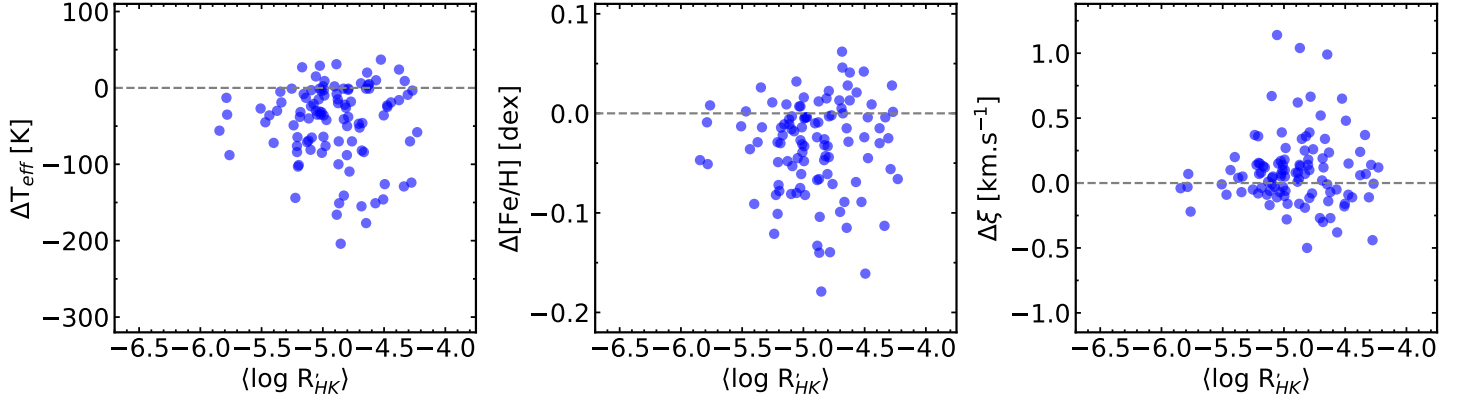


Figure 13. Differences (Δ) between effective temperatures, metallicities and microturbulent velocities determined without including Fe lines which are sensitive to activity (This study) and those determined including a significant number of activity sensitive Fe lines, as a function the mean activity index $\log R'_{\text{HK}}$ measured for the stars.

derived without sensitive lines. The mean differences (“non sensitive – sensitive”) and standard deviations are: -46 ± 51 K, -0.034 ± 0.047 , and 0.099 ± 0.277 km.s^{-1} for T_{eff} , metallicity, and microturbulent velocity, respectively. However, these are small differences which are of the order of the uncertainties in the derived parameters (see Table 5), which leads us to conclude that, based on the sample of Fe I and Fe II lines used here, there is no evidence (beyond the uncertainties) of a clear correlation between ΔT_{eff} , $\Delta[\text{Fe}/\text{H}]$ and $\Delta\xi$ with $\log R'_{\text{HK}}$.

Furthermore, if we segregate this sample into 3 regimes in terms of stellar activity (from Henry et al. 1996) we find that the mean T_{eff} , $[\text{Fe}/\text{H}]$ and ξ differences for the sub-samples of very inactive, inactive, and active stars are respectively -49 K, -0.035 dex, 0.063 km.s^{-1} ; -40 K, -0.038 dex, 0.128 km.s^{-1} ; and -47 K, -0.024 dex, 0.068 km.s^{-1} , again not showing a clear signature with $\log R'_{\text{HK}}$. The only signature to note is that the spread in ΔT_{eff} and $\Delta[\text{Fe}/\text{H}]$ increases for $\log R'_{\text{HK}} > \sim -5$. The 8 stars with the largest differences in T_{eff} ($> \sim 110$ K) all have $\log R'_{\text{HK}}$ larger than ~ -5.1 . This is also the case for the metallicity results shown in the middle panel of Figure 13: those stars with the largest variations in metallicity have $\log R'_{\text{HK}}$ larger than ~ -5 . In summary, very inactive stars display smaller spreads in ΔT_{eff} and $\Delta[\text{Fe}/\text{H}]$ when compared to the more active stars.

6. SUMMARY AND CONCLUSIONS

The results presented here were obtained through a spectroscopic analysis of a uniform set of high-resolution Keck I/HIRES spectra using a list of Fe I and Fe II lines, which yielded the fundamental stellar parameters of T_{eff} , $\log g$, ξ , and $[\text{Fe}/\text{H}]$, as well as stellar radii. The analysis employed the spectroscopic analysis code q^2 (Ramírez et al. 2014), which derives stellar parameters

semi-automatically. The sample includes 109 K2 stars, of which 75 have confirmed planets; the derived values of stellar radii were used to determine planetary radii. The Fe I and Fe II lines used in the analysis were from Yana Galarza et al. (2019) and consists of some lines that are sensitive to magnetic fields, as well as some lines that are insensitive. Main results are summarized below.

- Our stellar radii were combined with transit depths to calculate planetary radii for 93 confirmed planets orbiting 69 K2 stars. Most of transit depths were obtained from Kruse et al. (2019), with additional transit depths from Barros et al. (2016), Pope et al. (2016), and Christiansen et al. (2017). The internal precision of the planetary radii achieved here was 2.3% and the radius gap is detected in this sample of K2 planets, located at $R_{pl} \sim 1.9 R_{\oplus}$.

- Stellar activity using the S_{HK} index, which is defined by the fluxes of the Ca II H and K lines, was measured for 144 stars using spectra obtained from ExoFop and the KOA. The values of S_{HK} were derived using the equation in Isaacson & Fischer (2010), with a V-flux coefficient fit to values obtained for each spectrum, and were found to fall closely on the Mt. Wilson scale. Our derived values of S_{HK} as a function of $(B-V)_0$ follow the same trends as shown in Isaacson & Fischer (2010) and Boro Saikia et al. (2018). Photospheric contributions to S_{HK} were subtracted to obtain values of $\log R'_{\text{HK}}$ by using bolometric corrections from Rutten (1984) for main sequence and evolved stars.

- Our results for $\langle \log R'_{\text{HK}} \rangle$ as a function of rotational period for the K2 sample indicate that although activity, in general, decreases with increasing rotational period, there is a large scatter in the activity level for a given rotational period of ~ 0.5 dex in $\log R'_{\text{HK}}$; such a result has been noted previously, e.g., Böhm-Vitense (2007) and Metcalfe & van Saders (2017), and points to a com-

plex behavior in stellar activity that is related possibly to Rossby number (Metcalf & van Saders 2017).

- In a previous study of chromospheric activity in a sample of solar-type stars, Vaughan & Preston (1980) found a lack of F- and G-type stars with a intermediate activity levels, now called the “Vaughan-Preston gap”. This gap was confirmed by Henry et al. (1996) and Gomes da Silva et al. (2021) using a large sample of stars. Although we studied a much smaller sample of stars, our distribution of the mean values of $\log R'_{\text{HK}}$ also reveal the presence of the Vaughan-Preston gap.

- The possible impact of stellar activity on the derivation of the stellar parameters T_{eff} , $[\text{Fe}/\text{H}]$, and ξ (surface gravity is not expected to be sensitive to stellar activity) was investigated by including magnetically sensitive Fe I lines in a separate spectroscopic analysis.

We found systematic offsets between the two analyses with mean differences of “non sensitive – sensitive” of $\Delta T_{\text{eff}} = -46 \pm 51$ K, $\Delta[\text{Fe}/\text{H}] = -0.03 \pm 0.05$, and $\Delta\xi = +0.10 \pm 0.28$ km-s⁻¹. Although these systematic offsets are not significant and within the expected uncertainties, we note that the more active stars, with $\log R'_{\text{HK}} > -5.0$, exhibit larger scatter in their distributions of ΔT_{eff} and $\Delta[\text{Fe}/\text{H}]$ when compared to the quiet stars.

We thank the referee for detailed comments that helped improve the paper. V. L-T. acknowledges the financial support from Coordenação de Aperfeiçoamento de Pessoal de Nível Superior (CAPES). This research has made use of the NASA Exoplanet Archive, which is operated by the California Institute of Technology, under contract with NASA under the Exoplanet Exploration Program.

REFERENCES

- Asplund, M., Amarsi, A. M., & Grevesse, N. 2021, *A&A*, 653, A141, doi: [10.1051/0004-6361/202140445](https://doi.org/10.1051/0004-6361/202140445)
- Baliunas, S. L., Donahue, R. A., Soon, W. H., et al. 1995, *ApJ*, 438, 269, doi: [10.1086/175072](https://doi.org/10.1086/175072)
- Barros, S. C. C., Demangeon, O., & Deleuil, M. 2016, *A&A*, 594, A100, doi: [10.1051/0004-6361/201628902](https://doi.org/10.1051/0004-6361/201628902)
- Bensby, T., Feltzing, S., & Oey, M. S. 2014, *A&A*, 562, A71, doi: [10.1051/0004-6361/201322631](https://doi.org/10.1051/0004-6361/201322631)
- Berger, T. A., Huber, D., Gaidos, E., & van Saders, J. L. 2018, *ApJ*, 866, 99, doi: [10.3847/1538-4357/aada83](https://doi.org/10.3847/1538-4357/aada83)
- Böhm-Vitense, E. 2007, *ApJ*, 657, 486, doi: [10.1086/510482](https://doi.org/10.1086/510482)
- Boro Saikia, S., Marvin, C. J., Jeffers, S. V., et al. 2018, *A&A*, 616, A108, doi: [10.1051/0004-6361/201629518](https://doi.org/10.1051/0004-6361/201629518)
- Borucki, W. J. 2016, *Reports on Progress in Physics*, 79, 036901, doi: [10.1088/0034-4885/79/3/036901](https://doi.org/10.1088/0034-4885/79/3/036901)
- Borucki, W. J., Koch, D., Basri, G., et al. 2010, *Science*, 327, 977, doi: [10.1126/science.1185402](https://doi.org/10.1126/science.1185402)
- Bressan, A., Marigo, P., Girardi, L., et al. 2012, *MNRAS*, 427, 127, doi: [10.1111/j.1365-2966.2012.21948.x](https://doi.org/10.1111/j.1365-2966.2012.21948.x)
- Brown, E. L., Jeffers, S. V., Marsden, S. C., et al. 2022, *MNRAS*, 514, 4300, doi: [10.1093/mnras/stac1291](https://doi.org/10.1093/mnras/stac1291)
- Buder, S., Sharma, S., Kos, J., et al. 2021, *MNRAS*, 506, 150, doi: [10.1093/mnras/stab1242](https://doi.org/10.1093/mnras/stab1242)
- Castelli, F., & Kurucz, R. L. 2003, in *IAU Symposium*, Vol. 210, *Modelling of Stellar Atmospheres*, ed. N. Piskunov, W. W. Weiss, & D. F. Gray, A20. <https://arxiv.org/abs/astro-ph/0405087>
- Chahal, D., Kamath, D., de Grijs, R., Ventura, P., & Chen, X. 2023, *MNRAS*, 525, 4026, doi: [10.1093/mnras/stad2521](https://doi.org/10.1093/mnras/stad2521)
- Christiansen, J. L., Vanderburg, A., Burt, J., et al. 2017, *AJ*, 154, 122, doi: [10.3847/1538-3881/aa832d](https://doi.org/10.3847/1538-3881/aa832d)
- Ciardi, D. R., von Braun, K., Bryden, G., et al. 2011, *AJ*, 141, 108, doi: [10.1088/0004-6256/141/4/108](https://doi.org/10.1088/0004-6256/141/4/108)
- Cui, X.-Q., Zhao, Y.-H., Chu, Y.-Q., et al. 2012, *Research in Astronomy and Astrophysics*, 12, 1197, doi: [10.1088/1674-4527/12/9/003](https://doi.org/10.1088/1674-4527/12/9/003)
- da Silva, L., Girardi, L., Pasquini, L., et al. 2006, *A&A*, 458, 609, doi: [10.1051/0004-6361:20065105](https://doi.org/10.1051/0004-6361:20065105)
- de Leon, J. P., Livingston, J., Endl, M., et al. 2021, *MNRAS*, 508, 195, doi: [10.1093/mnras/stab2305](https://doi.org/10.1093/mnras/stab2305)
- Deleuil, M., Barge, P., Defay, C., et al. 2000, in *Astronomical Society of the Pacific Conference Series*, Vol. 219, *Disks, Planetesimals, and Planets*, ed. G. Garzón, C. Eiroa, D. de Winter, & T. J. Mahoney, 656
- Deleuil, M., Aigrain, S., Moutou, C., et al. 2018, *A&A*, 619, A97, doi: [10.1051/0004-6361/201731068](https://doi.org/10.1051/0004-6361/201731068)
- Demarque, P., Woo, J.-H., Kim, Y.-C., & Yi, S. K. 2004, *ApJS*, 155, 667, doi: [10.1086/424966](https://doi.org/10.1086/424966)
- Duncan, D. K., Vaughan, A. H., Wilson, O. C., et al. 1991, *ApJS*, 76, 383, doi: [10.1086/191572](https://doi.org/10.1086/191572)
- Egeland, R., Soon, W., Baliunas, S., et al. 2017, *ApJ*, 835, 25, doi: [10.3847/1538-4357/835/1/25](https://doi.org/10.3847/1538-4357/835/1/25)
- Epstein, C. R., Johnson, J. A., Dong, S., et al. 2010, *ApJ*, 709, 447, doi: [10.1088/0004-637X/709/1/447](https://doi.org/10.1088/0004-637X/709/1/447)
- ExoFOP. 2019, *Exoplanet Follow-up Observing Program - K2, IPAC*, doi: [10.26134/EXOFOP2](https://doi.org/10.26134/EXOFOP2)
- Fischer, D. A., & Valenti, J. 2005, *ApJ*, 622, 1102, doi: [10.1086/428383](https://doi.org/10.1086/428383)

- Flores, M., González, J. F., Jaque Arancibia, M., Buccino, A., & Saffe, C. 2016, *A&A*, 589, A135, doi: [10.1051/0004-6361/201628145](https://doi.org/10.1051/0004-6361/201628145)
- Fulton, B. J., & Petigura, E. A. 2018, *AJ*, 156, 264, doi: [10.3847/1538-3881/aae828](https://doi.org/10.3847/1538-3881/aae828)
- Fulton, B. J., Petigura, E. A., Howard, A. W., et al. 2017, *AJ*, 154, 109, doi: [10.3847/1538-3881/aa80eb](https://doi.org/10.3847/1538-3881/aa80eb)
- Gaia Collaboration, Prusti, T., de Bruijne, J. H. J., et al. 2016, *A&A*, 595, A1, doi: [10.1051/0004-6361/201629272](https://doi.org/10.1051/0004-6361/201629272)
- Gaia Collaboration, Brown, A. G. A., Vallenari, A., et al. 2021, *A&A*, 649, A1, doi: [10.1051/0004-6361/202039657](https://doi.org/10.1051/0004-6361/202039657)
- Gaia Collaboration, Vallenari, A., Brown, A. G. A., et al. 2023, *A&A*, 674, A1, doi: [10.1051/0004-6361/202243940](https://doi.org/10.1051/0004-6361/202243940)
- Ghezzi, L., Montet, B. T., & Johnson, J. A. 2018, *ApJ*, 860, 109, doi: [10.3847/1538-4357/aac37c](https://doi.org/10.3847/1538-4357/aac37c)
- Gomes da Silva, J., Santos, N. C., Adibekyan, V., et al. 2021, *A&A*, 646, A77, doi: [10.1051/0004-6361/202039765](https://doi.org/10.1051/0004-6361/202039765)
- Gonzalez, G. 1997, *MNRAS*, 285, 403, doi: [10.1093/mnras/285.2.403](https://doi.org/10.1093/mnras/285.2.403)
- Han, H., Wang, S., Bai, Y., et al. 2023, *ApJS*, 264, 12, doi: [10.3847/1538-4365/ac9eac](https://doi.org/10.3847/1538-4365/ac9eac)
- Han, S. I., Kim, Y. C., Lee, Y. W., et al. 2009, in *Globular Clusters - Guides to Galaxies*, ed. T. Richtler & S. Larsen, 33, doi: [10.1007/978-3-540-76961-3_9](https://doi.org/10.1007/978-3-540-76961-3_9)
- Hardegree-Ullman, K. K., Zink, J. K., Christiansen, J. L., et al. 2020, *ApJS*, 247, 28, doi: [10.3847/1538-4365/ab7230](https://doi.org/10.3847/1538-4365/ab7230)
- Henry, T. J., Soderblom, D. R., Donahue, R. A., & Baliunas, S. L. 1996, *AJ*, 111, 439, doi: [10.1086/117796](https://doi.org/10.1086/117796)
- Howell, S. B., Sobek, C., Haas, M., et al. 2014, *PASP*, 126, 398, doi: [10.1086/676406](https://doi.org/10.1086/676406)
- Huber, D., Bryson, S. T., Haas, M. R., et al. 2016, *ApJS*, 224, 2, doi: [10.3847/0067-0049/224/1/2](https://doi.org/10.3847/0067-0049/224/1/2)
- Ida, S., & Lin, D. N. C. 2004a, *ApJ*, 604, 388, doi: [10.1086/381724](https://doi.org/10.1086/381724)
- . 2004b, *ApJ*, 616, 567, doi: [10.1086/424830](https://doi.org/10.1086/424830)
- . 2005, *ApJ*, 626, 1045, doi: [10.1086/429953](https://doi.org/10.1086/429953)
- Isaacson, H., & Fischer, D. 2010, *ApJ*, 725, 875, doi: [10.1088/0004-637X/725/1/875](https://doi.org/10.1088/0004-637X/725/1/875)
- J. O'Meara. 2020, *KODIAQ Data Release 3*, IPAC, doi: [10.26135/KOA1](https://doi.org/10.26135/KOA1)
- Koch, D. G., Borucki, W. J., Basri, G., et al. 2010, *ApJL*, 713, L79, doi: [10.1088/2041-8205/713/2/L79](https://doi.org/10.1088/2041-8205/713/2/L79)
- Kruse, E., Agol, E., Luger, R., & Foreman-Mackey, D. 2019, *ApJS*, 244, 11, doi: [10.3847/1538-4365/ab346b](https://doi.org/10.3847/1538-4365/ab346b)
- Leighton, R. B. 1959, *ApJ*, 130, 366, doi: [10.1086/146727](https://doi.org/10.1086/146727)
- Livingston, J. H., Crossfield, I. J. M., Petigura, E. A., et al. 2018, *AJ*, 156, 277, doi: [10.3847/1538-3881/aae778](https://doi.org/10.3847/1538-3881/aae778)
- Loaiza-Tacuri, V., Cunha, K., Smith, V. V., et al. 2023, *ApJ*, 946, 61, doi: [10.3847/1538-4357/acb137](https://doi.org/10.3847/1538-4357/acb137)
- Lorenzo-Oliveira, D., Freitas, F. C., Meléndez, J., et al. 2018, *A&A*, 619, A73, doi: [10.1051/0004-6361/201629294](https://doi.org/10.1051/0004-6361/201629294)
- Majewski, S. R., Schiavon, R. P., Frinchaboy, P. M., et al. 2017, *AJ*, 154, 94, doi: [10.3847/1538-3881/aa784d](https://doi.org/10.3847/1538-3881/aa784d)
- Mamajek, E. E., & Hillenbrand, L. A. 2008, *ApJ*, 687, 1264, doi: [10.1086/591785](https://doi.org/10.1086/591785)
- Martinez, C. F., Cunha, K., Ghezzi, L., & Smith, V. V. 2019, *ApJ*, 875, 29, doi: [10.3847/1538-4357/ab0d93](https://doi.org/10.3847/1538-4357/ab0d93)
- Mayo, A. W., Vanderburg, A., Latham, D. W., et al. 2018, *AJ*, 155, 136, doi: [10.3847/1538-3881/aaadff](https://doi.org/10.3847/1538-3881/aaadff)
- Meléndez, J., Ramírez, I., Karakas, A. a. I., et al. 2014, *ApJ*, 791, 14, doi: [10.1088/0004-637X/791/1/14](https://doi.org/10.1088/0004-637X/791/1/14)
- Metcalfe, T. S., & van Saders, J. 2017, *SoPh*, 292, 126, doi: [10.1007/s11207-017-1157-5](https://doi.org/10.1007/s11207-017-1157-5)
- Mordasini, C., Alibert, Y., Benz, W., Klahr, H., & Henning, T. 2012, *A&A*, 541, A97, doi: [10.1051/0004-6361/201117350](https://doi.org/10.1051/0004-6361/201117350)
- Mordasini, C., Mollière, P., Dittkrist, K. M., Jin, S., & Alibert, Y. 2015, *International Journal of Astrobiology*, 14, 201, doi: [10.1017/S1473550414000263](https://doi.org/10.1017/S1473550414000263)
- Morris, B. M., Hawley, S. L., Hebb, L., et al. 2017, *ApJ*, 848, 58, doi: [10.3847/1538-4357/aa8cca](https://doi.org/10.3847/1538-4357/aa8cca)
- Nayakshin, S. 2010, *MNRAS*, 408, L36, doi: [10.1111/j.1745-3933.2010.00923.x](https://doi.org/10.1111/j.1745-3933.2010.00923.x)
- Noyes, R. W., Hartmann, L. W., Baliunas, S. L., Duncan, D. K., & Vaughan, A. H. 1984, *ApJ*, 279, 763, doi: [10.1086/161945](https://doi.org/10.1086/161945)
- Owen, J. E., & Murray-Clay, R. 2018, *MNRAS*, 480, 2206, doi: [10.1093/mnras/sty1943](https://doi.org/10.1093/mnras/sty1943)
- Persson, C. M., Fridlund, M., Barragán, O., et al. 2018, *A&A*, 618, A33, doi: [10.1051/0004-6361/201832867](https://doi.org/10.1051/0004-6361/201832867)
- Petigura, E. A., Crossfield, I. J. M., Isaacson, H., et al. 2018, *AJ*, 155, 21, doi: [10.3847/1538-3881/aa9b83](https://doi.org/10.3847/1538-3881/aa9b83)
- Pope, B. J. S., Parviainen, H., & Aigrain, S. 2016, *MNRAS*, 461, 3399, doi: [10.1093/mnras/stw1373](https://doi.org/10.1093/mnras/stw1373)
- Ramírez, I., Meléndez, J., Bean, J., et al. 2014, *A&A*, 572, A48, doi: [10.1051/0004-6361/201424244](https://doi.org/10.1051/0004-6361/201424244)
- Rampalli, R., Agüeros, M. A., Curtis, J. L., et al. 2021, *ApJ*, 921, 167, doi: [10.3847/1538-4357/ac0c1e](https://doi.org/10.3847/1538-4357/ac0c1e)
- Reinhold, T., & Hekker, S. 2020, *A&A*, 635, A43, doi: [10.1051/0004-6361/201936887](https://doi.org/10.1051/0004-6361/201936887)
- Rutten, R. G. M. 1984, *A&A*, 130, 353
- Seager, S., & Mallén-Ornelas, G. 2003, *ApJ*, 585, 1038, doi: [10.1086/346105](https://doi.org/10.1086/346105)
- Skumanich, A. 1972, *ApJ*, 171, 565, doi: [10.1086/151310](https://doi.org/10.1086/151310)
- Skumanich, A., Smythe, C., & Frazier, E. N. 1975, *ApJ*, 200, 747, doi: [10.1086/153846](https://doi.org/10.1086/153846)
- Snedden, C. A. 1973, PhD thesis, THE UNIVERSITY OF TEXAS AT AUSTIN.

- Sousa, S. G., Santos, N. C., Adibekyan, V., Delgado-Mena, E., & Israelian, G. 2015, *A&A*, 577, A67, doi: [10.1051/0004-6361/201425463](https://doi.org/10.1051/0004-6361/201425463)
- Spina, L., Nordlander, T., Casey, A. R., et al. 2020, *ApJ*, 895, 52, doi: [10.3847/1538-4357/ab8bd7](https://doi.org/10.3847/1538-4357/ab8bd7)
- Van Eylen, V., Agentoft, C., Lundkvist, M. S., et al. 2018, *MNRAS*, 479, 4786, doi: [10.1093/mnras/sty1783](https://doi.org/10.1093/mnras/sty1783)
- Vaughan, A. H., & Preston, G. W. 1980, *PASP*, 92, 385, doi: [10.1086/130683](https://doi.org/10.1086/130683)
- Vaughan, A. H., Preston, G. W., & Wilson, O. C. 1978, *PASP*, 90, 267, doi: [10.1086/130324](https://doi.org/10.1086/130324)
- Venturini, J., Guilera, O. M., Haldemann, J., Ronco, M. P., & Mordasini, C. 2020, *A&A*, 643, L1, doi: [10.1051/0004-6361/202039141](https://doi.org/10.1051/0004-6361/202039141)
- Vogt, S. S., Allen, S. L., Bigelow, B. C., et al. 1994, in *Proc. SPIE*, Vol. 2198, *Instrumentation in Astronomy VIII*, ed. D. L. Crawford & E. R. Craine, 362, doi: [10.1117/12.176725](https://doi.org/10.1117/12.176725)
- Wilson, O. C. 1968, *ApJ*, 153, 221, doi: [10.1086/149652](https://doi.org/10.1086/149652)
- Yana Galarza, J., Meléndez, J., Lorenzo-Oliveira, D., et al. 2019, *MNRAS*, 490, L86, doi: [10.1093/mnrasl/slz153](https://doi.org/10.1093/mnrasl/slz153)
- Yi, S., Demarque, P., Kim, Y.-C., et al. 2001, *ApJS*, 136, 417, doi: [10.1086/321795](https://doi.org/10.1086/321795)
- Yi, S. K., Kim, Y.-C., & Demarque, P. 2003, *ApJS*, 144, 259, doi: [10.1086/345101](https://doi.org/10.1086/345101)
- Zhang, W., Zhang, J., He, H., et al. 2022, *ApJS*, 263, 12, doi: [10.3847/1538-4365/ac9406](https://doi.org/10.3847/1538-4365/ac9406)